Event generator for nuclear collisions at intermediate energies

Denis Lacroix, Aymeric Van Lauwe, and Dominique Durand
Laboratoire de Physique Corpusculaire, ENSICAEN and Université de Caen, IN2P3-CNRS, Blvd du Maréchal Juin, 14050 Caen, France

(Received 20 November 2003; published 12 May 2004)

An event generator, HIPSE (heavy-ion phase-space exploration), dedicated to the description of nuclear collisions in the intermediate energy range is presented. Based on the sudden approximation and on geometrical hypothesis, it can conveniently simulate heavy-ion interactions at all impact parameters and thus can constitute a valuable tool for the understanding of processes such as neck emission or multifragmentation in peripheral or/and central collisions. After a detailed description of the ingredients of the model, first comparisons with experimental data collected by the INDRA Collaboration are shown. Special emphasis is put on the kinematical characteristics of fragments and light particles observed at all impact parameters for Xe+Sn reactions at 25 and 50 MeV/nucleon and Ni+Ni at 82 MeV/nucleon.

DOI: 10.1103/PhysRevC.69.054604 PACS number(s): 25.70.−z, 24.10.Lx, 25.70.Pq

I. INTRODUCTION: MOTIVATION OF THE PRESENT WORK

For several decades now, nuclear collisions in the intermediate energy range (say between 20 and 100 MeV/nucleon) have been used to explore the fundamental properties of nuclei under extreme conditions of pressure, temperature, and/or angular momenta (see, for instance, Ref. [1]). From an experimental point of view, large detection facilities—the so-called 4π detectors—have been developed to detect almost all emitted charged particles (see, for instance, Ref. [2]). Hence, complex events are recorded with, for instance, high multiplicities in central collisions. In view of the complexity of the processes occurring during the reaction, there are some difficulties to "reduce" the "raw" observables [these are mainly multiplicities, atomic numbers (sometimes mass numbers), energies, and/or velocities of emitted charged products and/or neutrons] into some well defined global characteristics of the collision. Nevertheless, this reduction (if possible) is a prerequisite to extract, for instance, the thermodynamical properties of the system under study. The problem very often arises from the fact that there are strong dynamical effects taking place at least in the first instants of the reaction.

As an example, let us take multifragmentation, defined as the emission in a short time scale of several species of atomic number larger than 2 [3] as compared to other decay mechanisms such as the formation of heavy residues or fission. Such a phenomenon is expected to be the ideal tool to study the transition from a liquidlike state (nuclei at normal density) towards a gaslike state associated with the vaporization of the system [4]. The quest for the signals of a nuclear phase transition of the liquid-gas type has led to rather sophisticated analyses. Such recent experimental analyses based on nuclear calorimetry have claimed evidence for a liquid-gas phase transition through the study of various signals [5–7]. Some of these analyses make extensive use of the thermal multifragmentation statistical models [8,9] to prove the existence of thermal equilibrium [10].

There are however some uncertainties in using statistical models. This is due to the lack of knowledge of dynamical effects, in particular, of the fast early processes which could eventually lead to the formation of equilibrated systems. In particular, the phase space explored during the collision is expected to be sensitive to the initial conditions of the reaction. Such a point is addressed in microscopic transport models [11–16]. These models provide a suitable framework for the description of nuclear collisions at intermediate energies and are able to describe dynamical effects. Unfortunately, although nucleon-nucleon collisions are included, one could not determine if the system has reached a complete thermal equilibrium. Moreover, there is not a direct link in such approaches between the outputs of the simulations and the thermodynamical properties of the excited species produced in the course of the reaction. As a consequence, these models do not give unambiguously important quantities required for statistical model calculations. For instance, internal excitation energies of the created fragments cannot be easily obtained in current microscopic calculations.

We believe that in between the two extreme approaches described above, namely, the statistical approach based on the reduction of the reaction to a few important parameters and the microscopic approach based on the transport theory, there is room for macroscopic-microscopic "phenomenology." This is the motivation for the work presented here in which we describe a phenomenological event generator allowing a detailed comparison with experimental data and accounting for both dynamical and statistical effects.

The paper is organized as follows. First, the main hypotheses of this work are outlined and the event generator [hereafter called the HIPSE (heavy-ion phase space exploration)] is described in Sec. II. A detailed comparison with experimental data is developed in Sec. III. Conclusions and perspectives are drawn at the end of the paper.

II. THE HIPSE EVENT GENERATOR: HYPOTHESIS AND DESCRIPTION

Following the hypothesis discussed above, we describe the reaction with help of three steps.

(a) The approaching phase of the collision ending

when the two partners of the reactions are at maximum overlap. This phase is considered by solving the classical equation of motion of the two partners in their mutual interaction potential. At that time, using the sudden approximation, the two nuclei in interaction are described by a collection of nucleons whose momentum and space distributions correspond to their ground-state boosted by the relative momentum and distance associated with maximum overlap between the two incoming nuclei.

(b) The partition formation phase: This phase corresponds to the rearrangement of the nucleons into several clusters and light particles (hereafter called the partition) according to the impact parameter of the reaction. The partition is built following coalescence rules in momentum and position spaces. The main consequence of this approximation is that the characteristics of the species produced in highly fragmented collisions will exhibit kinetic energy and angular distributions keeping a strong memory of the entrance channel.

(c) The exit channel and after-burner phase up to the detectors: The partition is propagated taking into account explicitly reaggregation effects due to the strong nuclear and Coulombic interactions among the various species of the partition. Since these latter are produced in excited states, secondary decays are taken into account by means of an evaporation code.

We now describe in detail these three stages.

A. The entrance channel

For a given beam energy E_B, a classical two-body dynamics during the phase of approach of the collision is assumed. Noting $V_{A_TA_P}(r=|\mathbf{r}_T-\mathbf{r}_P|)$ the interaction potential between the target and the projectile, we consider the evolution associated with the Hamiltonian $E_0=p^2/2\mu+V_{A_TA_P}(r)$, where $E_0=[A_T/(A_T+A_P)]E_B$ is the available energy in the center of mass while $\mathbf{p}$ is the relative momentum and $\mu=m_Tm_P/M$ is the reduced mass with m_T and m_P the target and projectile mass, respectively [18]. The concept of nuclear potential is rather unambiguously defined when the two nuclei are well separated. Then we use the proximity potential [19,20] with the parametrization of Ref. [17]. The promimity potential is not well suited for small relative distance $r \leqslant R_T+R_P$, where R_T and R_P are radii of, respectively, the target and the projectile. In this case, there is thus a need for another prescription defining nuclear potential between two strongly overlapping nuclei.

Such a potential is to a large extent unknown and should normally depend on different parameters describing the configurations of the system: shape, internal excitation energy, as well as the initial relative energy of the two partners [17]. In particular, the energy dependence can be understood by considering the two limiting approximations generally used to describe the nucleus-nucleus potential in fusion reaction, i.e., the *adiabatic* and the *sudden* approximations (see discussion in Ref. [21] and more recently in Ref. [22]). At very high relative energy, neglecting the influence of two-body collisions, we do expect that the internal degrees of freedom have no time to reorganize and that the system has a strong memory of the initial conditions.

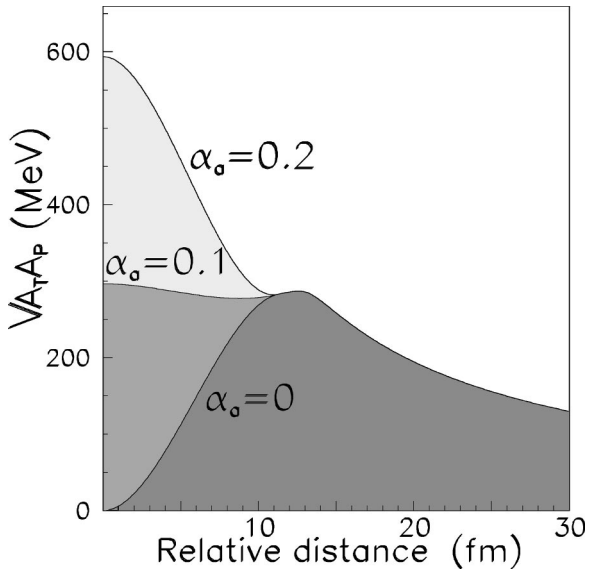

FIG. 1. Evolution of the nuclear potential $V_{A_TA_P}$ as a function of the relative distance for the ^{129}Xe+^{120}Sn system for $\alpha_a=0$, 0.1, and 0.2.

In view of these points, we do not expect a unique potential. As the beam energy increases, the internal degrees of freedom have less time to reorganize and the potential is expected to be sharper. We have included the possible energy dependence of the potential in a phenomenological way. In the following, we use a simple approximation for the construction of the potential. First, it is assumed that $V_{A_TA_P}$ depends on r uniquely even for small relative distances. In order to obtain the potential for $r<R_T+R_P$, we interpolate the potential between $r=0$ and $r=R_T-R_P$ using a third-order polynomial and assuming continuity of the derivative of the potential at each point. The value retained at $r=0$ is conveniently expressed as

$$V(r=0)=\alpha_a V^{\mathrm{Froz}}_{A_TA_P}(r=0),$$

where α_a is a parameter to be fixed by comparison with experimental data. $V^{\mathrm{Froz}}_{A_TA_P}(r=0)$ is the energy of the system assuming that the two densities of the system overlap completely in the frozen density approximation. In practice, we have tabulated once and for all $V^{\mathrm{Froz}}_{A_1A_2}(r=0)$ for all values A_1 and A_2 using the double folding approximation [21] with the simplified Skyrme interaction of Ref. [23] for the nuclear part of the interaction.

Examples of the potential obtained for $\alpha_a=0$, and 0.1, and 0.2 are displayed in Fig. 1 for the ^{129}Xe+^{120}Sn system. The evolution of the potential energy as a function of α_a gives the hardness of the potential in the phase of approach. According to our understanding of nuclear potential for the reactions close to the fusion barrier, α_a would be interpreted as a measure of the degree of reorganization of internal degrees of freedom during the reaction. However, more complex effects are expected in the beam energy regime we are considering. In our model, we will consider α_a as a free parameter which

represents the absence of knowledge of nucleus-nucleus potential at large overlap.

B. Building the partition

1. Sampling of the nucleons

At the minimum distance of approach, the two partners of the reaction overlap more or less according to the impact parameter and the value of the parameter α_a. At this point, the two nuclei are at maximum overlap. It is assumed that the reaction is fast compared to the time scale of reorganization of nucleonic single-particle degrees of freedom. Accordingly, the spatial and momentum distributions of the (A_T, Z_T) and (A_P, Z_P) nucleons constituting the target and the projectile are not expected to differ significantly from the ones they do have in the initial ground state of the two partners. In our model, we explicitly use this approximation, corresponding to the frozen density limit, to sample the positions and momenta of the nucleons in the center of mass of each partner of the reaction.

In order to have realistic density ground-state distributions, a semiclassical approximation [24] has been used. For a given nucleus, assuming spherical symmetry, the Thomas-Fermi energy is minimized under the constraint of proton and neutron number conservation. In practice, we have used the numerical method developed in Ref. [25] adapted to the Seyler-Blanchard parametrization of the force derived in Ref. [26]. Using a Metropolis algorithm, a set of (A_T, Z_T) and (A_P, Z_P) nucleons is sampled. In addition, the Pauli principle is roughly taken into account in each nucleus by imposing that $\Delta r_\tau \Delta p_\tau \geqslant \hbar$, where Δr_τ and Δp_τ are the relative position and momentum of two nucleons with same isospin $\tau = n$ or p belonging to the same nucleus. This procedure ensures a uniform arrangement of the nucleons in each nucleus. At this stage, a set of $A_T + A_P$ nucleons with position (x_i, y_i, z_i) and momentum $(p_{x_i}, p_{y_i}, p_{z_i})$ in the center-of-mass frame of the reaction is obtained. A final (small) correction is applied to the position and momentum of the nucleons in order to keep the position and momentum of the center of mass constant.

2. Defining the quasiprojectile and the quasitarget fragments

For finite impact parameters, our approach is mainly based on geometrical hypotheses: Those nucleons which do not lie inside the overlap region constitute the so-called quasiprojectile (QP) and quasitarget (QT) fragments. The overlap region is defined as follows: for a nucleon initially in the target, we assume that it is in the overlap region if $|\mathbf{r}_i - \mathbf{r}_P| \leqslant R_P$, where $\mathbf{r}_P$ is the position of the projectile in the center of mass frame, while R_P is the equivalent sharp radius taken from Ref. [27]. For nucleons initially in the projectile we used the same criteria with respect to the target.

Such a definition corresponds to the so-called participant-spectator picture. However, it is experimentally observed that strong deviations from such a simplified approach have been observed in the energy regime considered here. In particular, quasitarget and/or quasiprojectile fragments have kinetic energies which are slightly reduced with respect to the initial projectile and target ones. This effect can be taken into account by the exchange of particles between the two partners during the reaction. In our model, this is introduced "by hand" by assuming that a fraction x_{tr} of the nucleons coming initially from the target (projectile) and belonging to the overlap region are transferred to the projectile (target). Again, we do expect that the number of transferred nucleons decreases with the beam energy and thus that x_{tr} depends on the initial energy.

3. Building clusters from nucleons

We now consider the nucleons located inside the overlap region. They constitute a reservoir for building clusters at midrapidity. Experimentally, it is observed that a large number of detected nucleons and light particles at midrapidity are issued from the deexcitation of sources initially produced in the overlap zone. However, when the beam energy increases (above the Fermi energy), another contribution sets in corresponding to the preequilibrium emission of light particles with large transverse momenta. These particles are generally assigned to promptly emitted particles induced by hard nucleon-nucleon collisions. Guided by this observation, we assume that a percentage of nucleon-nucleon collisions (noted x_{coll}) occurs. Thus, some nucleons in the overlap region encounter collisions. For simplicity, we separate explicitly the formation of fragments built from nucleons that have suffered no collisions from the formation of fragments produced with collided nucleons. Let us first consider the method used to create fragments starting from the nucleons that have experienced no hard collisions. In order to create fragments from nucleons, we use the following coalescence algorithm. First, one of the nucleons is chosen at random and it constitutes a *coalescence point* from which a fragment is built. Let $A_1 = 1$ be its mass number, $\mathbf{R}_1$ its position, and $\mathbf{P}_1$ its momentum. Another nucleon i in the overlap region is chosen at random. The nucleon i can be captured by the cluster labeled 1 according to the two following criteria.

(1) Existence condition: We first test if the composite nucleus is known (in particular, its binding energy) by checking its presence in an experimental mass table.

(2) Position and momentum conditions: It is expected that only nucleons that are close enough in phase space to the considered fragment can be absorbed. The exact conditions for which a nucleon in a nuclear medium can be absorbed by a fragment are poorly known. However, a simple phenomenological criterion can be introduced as follows. If we take r_i and p_i as the position and momentum of the nucleon with respect to the fragment, the following condition is used:

$$\frac{p_i^2}{2m} + \frac{V_{\mathrm{cut}}}{1 + \exp\left[\dfrac{(r_i - d_f)}{a}\right]} < 0, \tag{1}$$

where m is the nucleon mass. The parameters d_f and V_{cut} correspond to cuts in r space and p space. The distance d_f is a direct cutoff in r space. It is written as $d_f = R_f + r_{\mathrm{cut}}$, where R_f is the equivalent sharp radius of the fragment while r_{cut} is a parameter kept constant throughout the paper. The parameter V_{cut} is a cutoff in momentum space independent of the

considered nucleus. In practice, we adjusted the values to reproduce experimental data, we obtained $r_{\mathrm{cut}}=2.5$ fm. Using $V_{\mathrm{cut}}=-p_{\mathrm{cut}}^2/2m$, we obtained $p_{\mathrm{cut}}=500$ MeV/c and a diffuseness parameter fixed arbitrarily to $a=0.6$ fm.

If the two preceding conditions are fulfilled, the nucleon is absorbed by the fragment and the position and momentum of the cluster of mass $A_1=2$ is recalculated according to the positions and momenta of its constituents. If one of the conditions is not met, the nucleon serves as a new *coalescence point*. A new nucleon is then chosen from the remaining nucleons and the procedure is iterated. The position, momentum, mass, and charge of the chosen fragment are then updated at each step. The aggregation procedure stops when all available nucleons have been considered. If at a given step there is more than one possibility for the aggregation, the nucleon is absorbed by one of the fragments which is randomly chosen.

4. Nucleon-nucleon collisions

An increase of the effect of nucleon-nucleon collisions is expected when the beam energy increases. In the present model, a percentage x_{coll} of nucleon-nucleon collisions is assumed. Noting A_{over} the number of nucleons in the overlap region, the number of collisions is thus defined by $N_{\mathrm{coll}}=x_{\mathrm{coll}}A_{\mathrm{over}}$. Such collisions tend to wash out the memory of the entrance channel and may eventually lead to the formation of a compound nuclear state. Thus, we do expect that these collisions distort more or less the initial Fermi distribution of the nucleons and lead to a slight modification of the properties of promptly emitted particles and light clusters.

A full treatment of nucleon-nucleon collisions either in the weak [28] or strong coupling regime such as intranuclear cascade [29] is clearly out of the scope of the present work. In our model, we use the following simplified procedure.

In the course of a two-body collision, the two particles exchange momentum, while in r-space, a complete loss of the memory of the positions before collisions is explicitly assumed. The new positions of the two particles are supposed to be randomly distributed inside a sphere of radius $R_{\mathrm{coll}}=1.2A_{\mathrm{over}}^{1/3}+r_{\mathrm{coll}}$. The parameter r_{coll} is taken sufficiently large to enable the particles to escape rapidly the dense matter. We used a value of $r_{\mathrm{coll}}=4$ fm to reproduce the experimental data. Note, however, that, due to the Pauli exclusion principle, not all the sphere of radius R_{coll} is accessible. We have treated roughly this effect by restricting the accessible phase space of the nucleons after collisions and assuming that they could not be placed inside the quasitarget and quasiprojectile. This assumption is essential to correctly reproduce the experimental data and, in particular, the excess of particles at large transverse momenta.

After the N_{coll} collisions, we use a separate coalescence algorithm following the same procedure as the one described in the preceding section. However, it appears, in practice, that two modifications are required in order to correctly reproduce the experimental rate of particles and light fragments. First, after the coalescence of a nucleon by a fragment, the position of the new fragment is not deduced from the one of its constituent but is also chosen randomly as we did for the particles after a collision. Second, a larger value of r_{cut}, taken equal to 7 fm, is retained for the "link" condition in Eq. (1). This large value in our model could be interpreted as a larger correlation between nucleons after collision in forming a cluster compared to the case without collisions. It is also possible that other more complex effects such as direct knock-out of preformed light clusters occur. Therefore, it may be that this large value is an artificial way to mimic such complex phenomena.

5. Summary

Considering these different steps, we end up with a set of N_{frag}^{ini} fragments (including the QP and QT) with mass number, position, momentum, and angular momentum $(A_f,\mathbf{R}_f,\mathbf{P}_f,\mathbf{L}_f)$ by considering the characteristics of the nucleons belonging to each fragment. At that point, a "clock" is started corresponding to $t=0$ fm/c for the forthcoming dynamics. Note that the number of fragments is not fixed *a priori* at variance with the work described in Ref. [30]. These fragments constitute a partition. They are created in a high density region and are initially strongly overlapping. This is largely in contrast with the standard assumption made in thermal models stating that fragments are created at low density following a thermal or mechanical expansion [8,9].

C. Final state interaction and the reaggregation phase

The difficulty to produce partitions at high density lies in the need to treat as well as possible strong nuclear final state interaction. Indeed, because fragments can overlap during times comparable to the reaction time (typically a few tens of fm/c), there is a need to propagate the partition before freeze-out is reached. This is first achieved during a time of 50 fm/c according to the Hamiltonian

$$H=\sum_i \frac{P_i^2}{2mA_i}+\sum_{i<j}\mathbf{V}_{A_iA_j}(|\mathbf{R}_i-\mathbf{R}_j|). \tag{2}$$

For the sake of continuity and consistency, the same interaction potentials as for the entrance channel part of the reaction are used. However, for protons or neutrons interacting with nuclei, we used standard Woods-Saxon potential for the nuclear part of the interaction.

At that time an important reorganization in spatial and momentum configuration may have occurred. It leads generally to less compact configurations. It however may happen that two fragments cannot separate because their relative energy is lower than the fusion barrier. In that case, the two nuclei fuse and the properties of the fused system are calculated accordingly. This possibility of fusion is important for two reasons. First, it avoids that two fragments orbit in their mutual field up to the final steps of the propagation. Second, it allows one to explore a variety of reaction mechanisms that are beyond the modified participant-spectator picture that is used in the first stage of the model. For instance, at very low incident energy, most of the fragments produced in highly fragmented partition will fuse possibly producing a single composite system. Thus according to the incident energy, the reaggregation phase implemented in our approach allows one to smoothly explore mechanisms between com-

plete or incomplete fusion up to the pure participant-spectator picture. Moreover, since fragments are produced with nucleons whose characteristics have a strong memory of the entrance channel, preequilibrium effects can be described in the framework of our model.

After this first propagation at high density and the reaggregation phase, we end up with a partition of N_{frag} fragments whose kinematical characteristics have been updated. The procedure described above ensures that no recombinations of clusters are possible after this stage. From now on, the interaction between the fragments is purely Coulombic. However, it is expected that the fragments emerge from the reaction with a sizable excitation energy. It is then assumed that the thermalization of the nucleons inside each fragment occurs on a time scale of the order of a few tens of fm/c after the reaggregation. Further decay of such excited fragments is described by means of a statistical evaporation code. Since the thermalization is not described at the microscopic level, the estimation of the excitation energy can only be obtained with help of a global energy balance of the reaction.

D. Determining the excitation energy of the fragments inside the partition

After the reaggregation phase described above, the total energy balance in the center-of-mass frame reads

$$E_0 = Q + E_K + E_{\mathrm{pot}} + E^* + E_{\mathrm{rot}}, \tag{3}$$

where E_K and E_{pot} are, respectively, the sum of the kinetic and potential energies of the fragments, E_{rot} is the sum of their rotational energies, and Q is the mass energy balance between the entrance channel and the considered partition. In our calculation, the rotational energy is estimated by assuming rigid spheres for the fragments.

Finally, the quantity E^* corresponds to the total excitation energy. Note that, if the quantity E^* is negative, the partition is rejected since it then corresponds to unaccessible phase space according to the initial available energy. The total excitation energy must be shared among fragments. Due to the very discrete nature of excited states in light nuclei at least at low excitation energy, these latter are considered separately from medium and heavy nuclei. The following procedure has been used.

(1) For light nuclei ($Z_f < 6$), the excitation energy is first estimated by assuming proportionality to the number of nucleons in the considered fragment: $E_f^* = E^* A_f / A$, where A is the total mass number. For light fragments, a table of discrete excited state energies and the associated decay channels has been used. If the estimated excitation energy of the fragment is below the highest experimentally known discrete excited state, a discrete state is populated statistically with help of a Boltzmann factor according to the estimated temperature T using $E_f^* = aT^2$ with $a = A/10$. In opposite, the estimated excitation energy is taken as the "true" value if it lies above the last known discrete state. In such a case, all possible decay channels are considered during its deexcitation.

(2) After considering all light fragments, an amount E_H^* of excitation energy remains to be shared among medium and heavy fragments. For those, two methods of repartition of excitation energy have been tested. In the first one, similar to light nuclei, we assume that the excitation energy is proportional to the mass number of the fragment, thus leading to $E_f^* = E_H^* A_f / A$. The second method is based on the assumption that E_f^* should be related with the internal motion of the nucleons inside the fragments. Thus, for each fragment, we have calculated the mean internal kinetic energy of the nucleons:

$$E_{\mathrm{int}}^f = \sum_{i \in f} \frac{(\mathbf{p}_i - \mathbf{P}_f / A_f)^2}{2m}.$$

The quantity $x_f = (E_{\mathrm{int}}^f / A_f) / \Sigma_f (E_{\mathrm{int}}^f / A_f)$ is defined for each fragment (the sum runs over all $Z \geqslant 6$) and the following prescription has been used to share E_H^* among the fragments: $E_f^* = x_f E_H^*$.

It is interesting to note that although very different, the two procedures lead to very similar results.

E. The after-burner phase: The evaporation stage

At this stage, the partition is ready for the after-burner phase, which consists in propagating the fragments in the overall Coulombic field and considering secondary decays. The decay is achieved using the SIMON event generator [31]. In particular, the decay in flight of excited species is considered in order to preserve space-time correlations. It is important to note that the SIMON code takes into account all possible decay channels from neutron evaporation up to symmetric fission. Therefore, in our approach, fragments and light particles are produced at all time scales from the very early instants of the collision (before 50 fm/c) up to several thousand fm/c.

Examples of partition in space configuration for different impact parameters and time of the reaction from peripheral to central collisions are shown in the left part of Fig. 2. In the middle panel of the figure, the nuclei partition before and after the reaggregation is shown. This figure testifies that a large fraction of light nuclei is issued from the very first instant of the collision in the overlap region. It is also clear that final state interactions play a significant role. Finally, in the right side of Fig. 2, an intermediate stage during the deexcitation is presented, illustrating the possible in-flight statistical emissions of different species.

F. Discussion on the inputs of the model

The schematic model we are presenting here contains many inputs such as proximity potentials [17] or fission barriers [32] for the deexcitation part of the model. All these inputs represent the status of our actual macroscopic knowledge of nuclei adjusted to reproduce at best properties of a large variety of nuclei. In our model, we took the same parameters as those of the original works.

Conjointly, we have introduced phenomenological parameters, such as range in r space and p space for fragment formation which are supposed to mimic a fast reorganization of the nucleonic degrees of freedom leading to fragmentation. These parameters have been adjusted at once and are being kept fixed in all applications. After that, we end with a

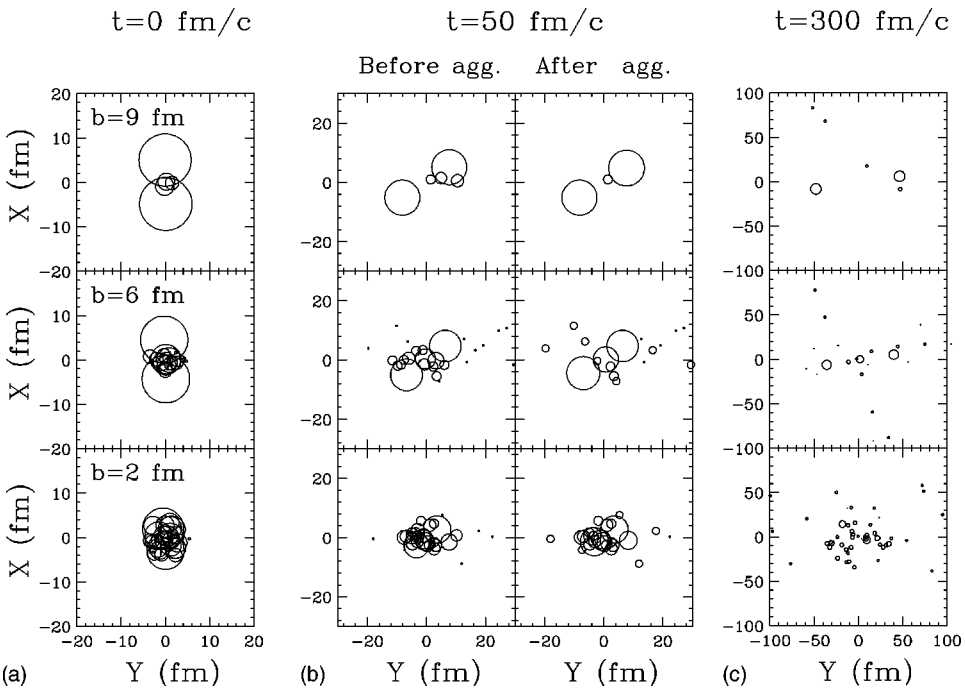

FIG. 2. Example of nuclear dynamics obtained for the reaction ^{129}Xe+^{120}Sn at $E=50$ MeV/nucleon. From top to bottom, the initial impact parameters $b=9$ fm, $b=6$ fm, and $b=2$ fm are presented. In each case, from left to right figures correspond to the initial cluster configuration ($t=0$ fm/c), the configuration before and after the reaggregation ($t=50$ fm/c), and during the deexcitation ($t=300$ fm/c).

model where only three important parameters remain: the percentage of nucleons transferred, $x_{\rm tr}$, between the projectile and target, the parameter α_a which describes the hardness of the potential, and the percentage of nucleon-nucleon collisions, $x_{\rm coll}$.

In the following, the values of the parameters have been adjusted by comparing the results of the calculation with experimental data. The data used for the study have been collected by INDRA Collaboration near the GANIL facility [33] (and references therein) for Xe+Sn collisions at 25 MeV/nucleon and 50 MeV/nucleon and Ni+Ni at 32, 52, and 82 MeV/nucleon [34]. Calculations were also performed for Xe+Sn at 80 MeV/nucleon and compared with data taken by INDRA-ALADIN Collaboration at the SIS facility [35]. Results will be published elsewhere [36]. We present in Fig. 3 the evolution of the parameters as a function of the beam energy. As expected, α_a and $x_{\rm coll}$ increase with E_B while the number of transferred nucleons decreases. It is worth noting that a similar set of parameters was used for Xe+Sn and Ni+Ni and a clear systematic evolution of the parameters observed, which approximately scales with the size of the colliding nuclei for symmetric systems. In the following, we will only show comparisons between the results of the model and data for Xe+Sn at 25 MeV/nucleon and 50 MeV/nucleon and Ni+Ni at 82 MeV/nucleon. For other energies, similar agreement has been found.

III. COMPARISON WITH EXPERIMENTAL DATA

A. "Raw" outputs of the model

Before going on with a detailed comparison of the model outputs with experimental data, it is worth having an overview of the characteristics of the reaction as simulated by HIPSE. To this end, we show in Fig. 4, the bidimensional atomic number Z vs the reduced parallel velocity $v_{//}/v_{\rm proj}$ for the reaction ^{129}Xe+^{120}Sn at 50 MeV/nucleon displayed as a function of the reduced impact parameter $b_{\rm red}$ defined as $b/b_{\rm max}$. Note that only nuclear species with $Z\geqslant 3$ are shown in the figure. The first panel corresponds to all events and, as

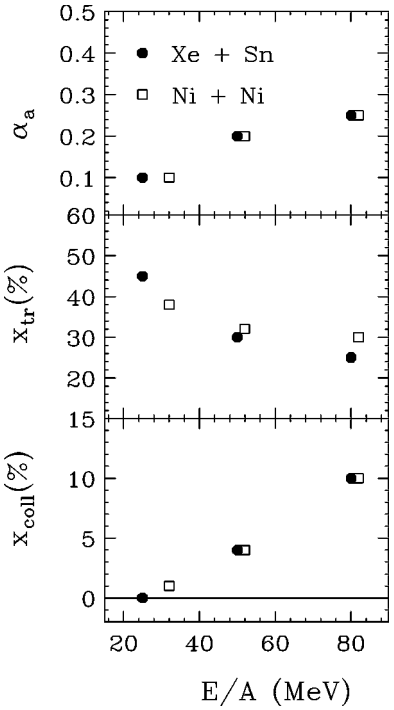

FIG. 3. Values of the different parameters of the model as a function of the beam energy for the reaction ^{129}Xe+^{120}Sn (filled circles) and ^{58}Ni+^{58}Ni (squares). From top to bottom, we present, respectively, the evolution of the parameter associated with the potential hardness α_a, the rate of exchange of particles between the target and projectile, $x_{\rm tr}$ (in percent), and the percentage of nucleon-nucleon collisions in the overlap region, $x_{\rm coll}$ (in percent).

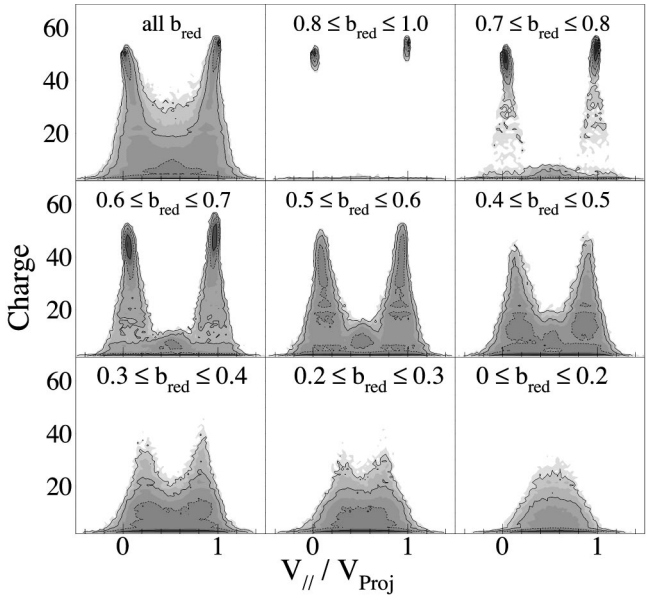

FIG. 4. Bidimensional Z-$v_{//}/v_{proj}$ for the reaction $^{129}Xe+^{120}Sn$ at 50 MeV/nucleon as given by the HIPSE event generator. Each panel is associated with a reduced impact parameter range indicated on top of the panel. For the sake of clarity, only $Z \geqslant 3$ have been considered.

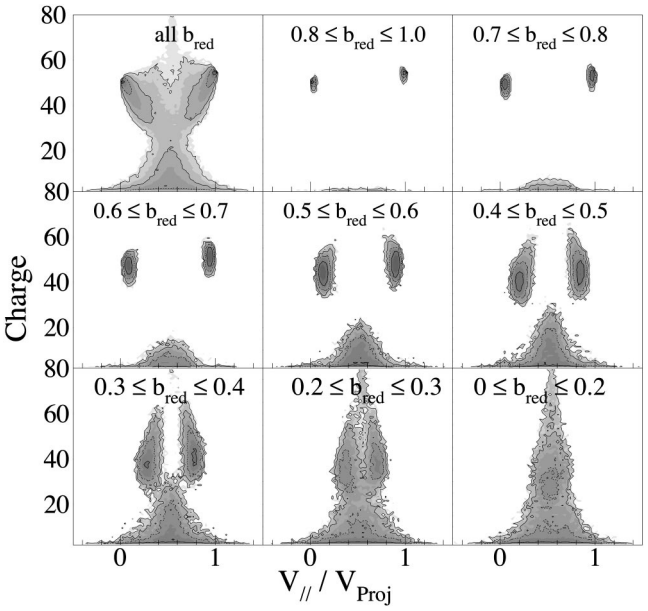

FIG. 5. Same as Fig. 4 for fragments created after the reaggregation phase and before the deexcitation.

such, is dominated by large impact parameters. Thus, two large contributions associated with the QP and the QT close to the loci of the projectile and target are evidenced with a slight velocity damping as Z decreases. This is followed by a contribution centered around midrapidity dominated by IMF's
(Z between 3 and 10). The evolution as a function of b_{red} displayed in the other panels testifies the geometrical nature of the reaction as simulated by HIPSE. At large b_{red} (until $b_{red} \simeq 0.8$), the reaction remains essentially binary, dominated by the contribution of the QP and the QT with a (small) contribution limited to $Z=3$ in the overlap region. Around $b_{red} \simeq 0.7$, the symmetric fission channel opens up with a rather low probability. Gradually, the size of the QP and of the QT decreases with b_{red} as a consequence of the geometrical assumption used in the model. Their contribution vanishes almost completely for $b_{red} \leqslant 0.3$. In parallel, the contribution of the overlap region increases to become dominant. Note however that even for central collisions, the parallel velocity distribution is very large, extending up to the beam and target velocities. In our model, parallel velocity fluctuations may have two origins. Part of the fluctuations are due to the inherent kinetic energy fluctuations occurring from the statistical decay of hot clusters. However, in our model, most of the fluctuations arise from those of the initial partition after reaggregation. This is indeed illustrated in Fig. 5 where the reduced parallel velocity $v_{//}/v_{proj}$ before the deexcitation phase is presented for the same reactions as in Fig. 4. In this figure, we clearly see that the initial fluctuations are large and already contain most of the fluctuations displayed in Fig. 4.

The evolution of the charge distribution after deexcitation as a function of the impact parameter, Fig. 6, shows the rather abrupt transition from a distribution dominated by the QP and the QT at $b_{red} \geqslant 0.6$ towards a monotonous distribution for $b_{red} \leqslant 0.5$. The charge distribution before deexcitation (light gray) has also been superimposed. Notice that, even in central collisions, heavy fragments are produced before secondary decay. However, while at large impact parameters, heavy nuclei (mainly QP and QT) survive to the afterburner stage, in more central collisions, they are systematically disintegrated into lighter nuclei or particles. This is due to the initial internal excitation energy which significantly increases with the centrality of the reaction.

The mean evolution of E^*/A as a function of b_{red} is displayed in Fig. 7. As expected, the excitation energy deposited

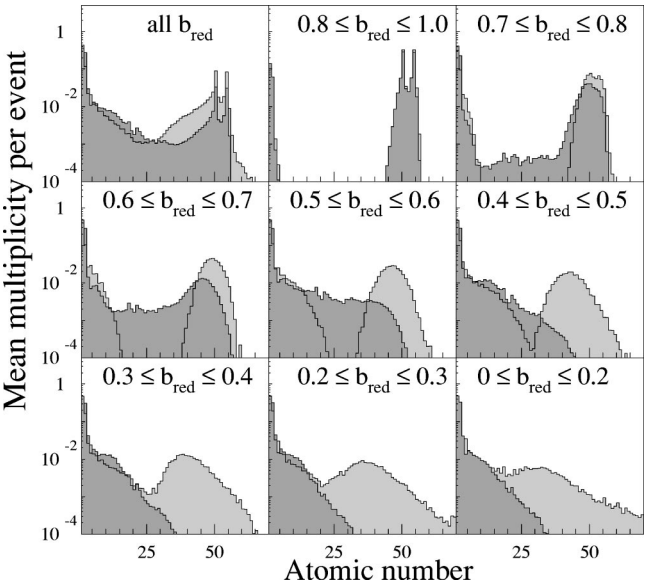

FIG. 6. Same as Fig. 4 but for the atomic number distribution. In light gray, we present the initial charge distribution while dark gray corresponds to the distribution after deexcitation.

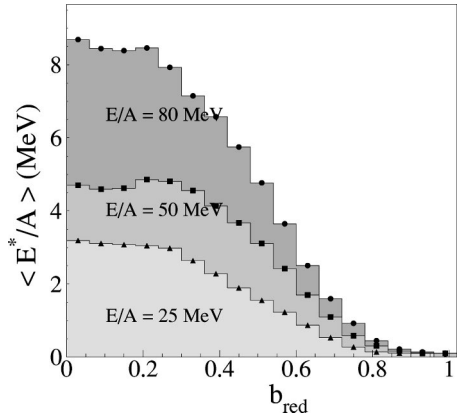

FIG. 7. Mean total initial excitation energy [given by Eq. (3)] vs reduced impact parameter b_{red} for Xe+Sn at 25, 50, and 80 MeV/nucleon.

in fragments increases with the initial available energy reaching values $\langle E^* \rangle / A \simeq 3$, 5, and 8 MeV/nucleon, respectively, for central collisions ($b_{red} < 0.4$) at 25, 50, and 80 MeV/nucleon.

B. Survey of the experimental data

The model described above is now compared with experimental data taken by INDRA Collaboration at the GANIL facility. In order to test the model at various impact parameters, three different cuts have been applied to the data. These cuts are more and more severe and, as such, they sample more and more central collisions.

(a) Minimum bias events: these are events where at least 10% of the total charge and total linear momentum along the beam axis (for charged particles) have been detected. This selection is dominated by large impact parameter collisions.

(b) "Complete" events: the second selection of the data has been performed using the completeness criterium that has been mostly used by INDRA Collaboration. It requires that at least 80% of the total charge and total linear momentum (for charged particles) be detected. This corresponds to midcentral and central collisions for which fragmentation is a dominant decay mechanism.

(c) "Complete central" events: in addition to the preceding completeness criterium, a sorting is applied by means of an additional global variable. A momentum tensor analysis is developed. The diagonalization of the tensor gives three eigenvalues on the basis of which several sorting variables may be defined. Here, we have used the so-called flow angle θ_{flow} that corresponds to the angle between the main axis of the tensor and the beam axis. For more details, see Ref. [37]. It is generally expected that large values of the flow angles correspond to more violent collisions and thus select smaller impact parameters. In the following, we have considered events with $\theta_{flow} > 30°$.

C. Impact parameter sorting and relation with the θ_{flow} selection

We first show in Fig. 8 the simulated θ_{flow} distributions for complete events for ^{129}Xe+^{120}Sn reactions at 25 and

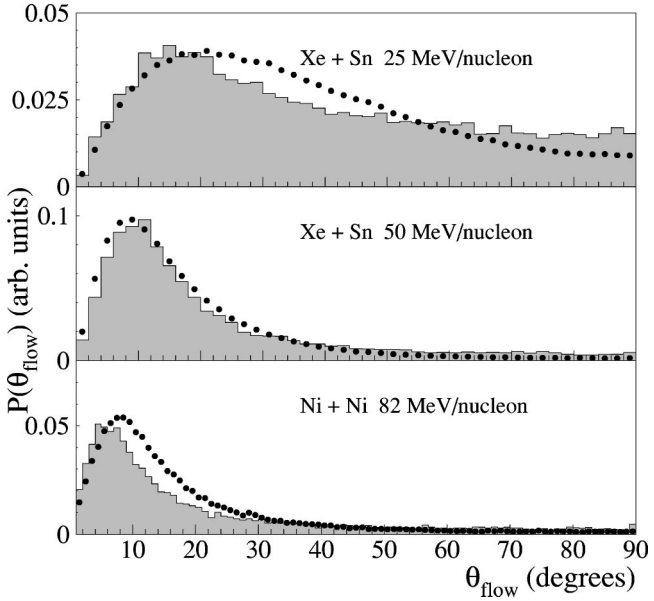

FIG. 8. Distributions of experimental (full circles) and calculated (histogram) θ_{flow} for ^{129}Xe+^{120}Sn reactions at 25 MeV/nucleon (top), 50 MeV/nucleon (middle), and Ni+Ni at 82 MeV/nucleon (bottom). Data have been selected with help of criterium (b) (see text).

50 MeV/nucleon and ^{58}Ni+^{58}Ni at 82 MeV/nucleon after filtering of the calculation with help of the software filter of the INDRA detector [38]. These distributions are compared with the corresponding experimental data (black points). A reasonable agreement with the data is obtained although a sizable deviation appears for the highest incident energy considered in this work.

The overall agreement of the model with the data as far as the flow angle distribution is concerned allows us to consider safely the event selection used in this work and provides a convenient framework for a detailed comparison between the model and the experimental data. Figure 9 shows the impact parameter distributions associated with the three selections in

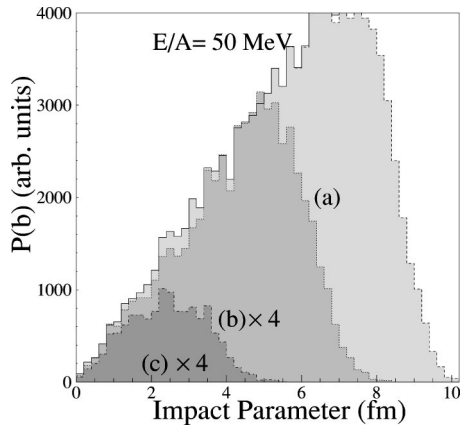

FIG. 9. Impact parameter distributions for the reaction ^{129}Xe +^{120}Sn at 50 MeV/nucleon as given by the model. Unfilled histogram: all simulated events. Other histograms are labeled according to the selection discussed in the text. Note that, in cases (b) and (c) the distributions have been multiplied by a factor 4.

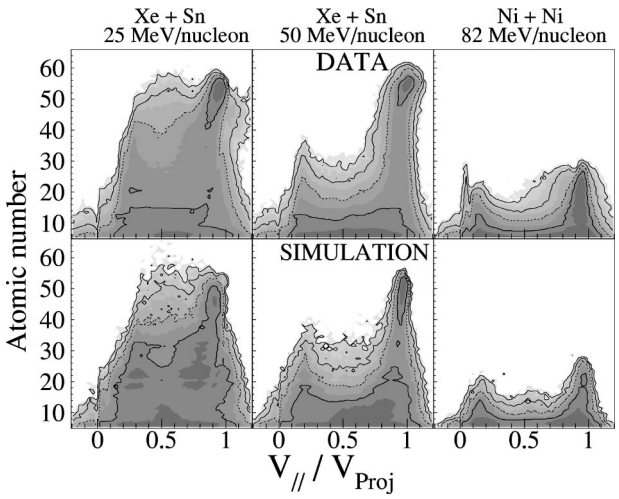

FIG. 10. Three-dimensional plots (in log scale) $v_{//}/v_{\mathrm{proj}}$-Z. Top panels are for experimental data while bottom panels are for simulated data. Event selection corresponds to case (a) (see text). Only fragments with atomic numbers larger than or equal to three are included in the figure.

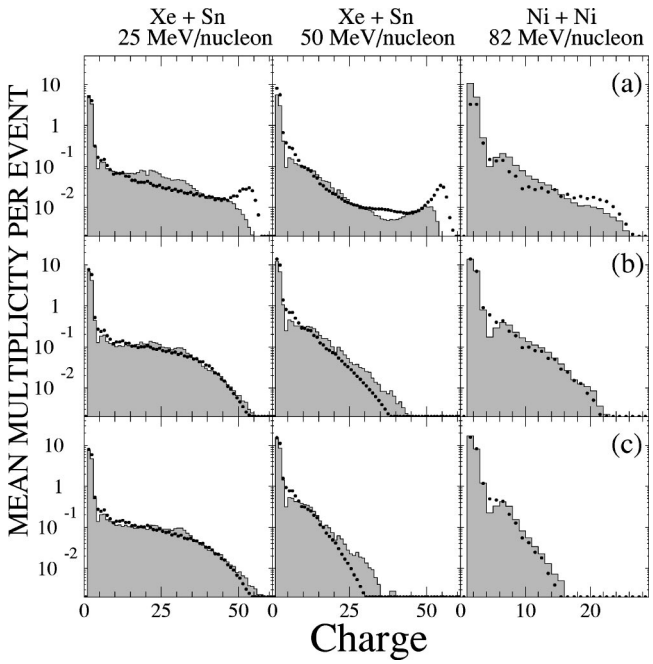

FIG. 11. Experimental (black points) and calculated (filled histograms) atomic number multiplicity per event for the reactions indicated on top of each panel. Top, event selection (a); middle, event selection (b); bottom; event selection (c).

the 50 MeV/nucleon case. As expected, selection (a) is associated with the full range of impact parameters up to the grazing angle although, there, the geometrical acceptance of the
INDRA detector is limited and thus reduces strongly the number of events. Samples (b) and (c) are associated with more central collisions. Note also that the completeness criterium induces a rather strong reduction factor in the event acceptance.

D. Atomic number and kinetic energy distributions

A convenient observable to address the kinematics and the topology of the reaction is the bidimensional correlation between the atomic number and the parallel velocity of all emitted fragments as displayed in Fig. 10. The general trends of the experimental data are reproduced by the simulation. Fragments with atomic numbers close to the projectile exhibit velocities close to the beam velocity as expected. The slight slowing down of the quasiprojectile as its atomic number decreases is correctly accounted by the model. As already discussed, this effect is considered by transferring nucleons from the participant zone towards either the QP or the QT. However, as beam energy increases, nucleon exchange and final state interaction effect decrease. This is the transition between fully damped reactions at low energy towards the pure participant-spectator picture at relativistic energies. Note the lack of symmetry between the kinematics of the QP and the QT, which is due to experimental threshold effects that prevent the detection of slow heavy fragments. A sizable amount of matter is emitted near midrapidity. This is due to the production of fragments in the overlap region of the reaction as already discussed before. Since they are produced by a random mixing of nucleons originating both from the target and the projectile, their distribution is centered at midrapidity since we deal with symmetric systems. However, the internal motion of the nucleons and the final state interaction induce large fluctuations in the final velocities of the fragments originating from the overlap region. In addition, fragments with $Z \simeq 3-6$ may be evaporated by the QP and the QT: this is the contribution located around $v_{//}/v_{\mathrm{proj}} \simeq 0.8-0.9$ in the continuity of the QP and QT branches.

Figure 11 shows the experimental atomic number mean multiplicity per event (black points) compared to the results of the calculation (solid line) after filtering. The three selections are presented at different beam energies. Although far from perfect, a correct agreement between the model and the data is reached. In particular, the evolution of the shape of the distributions as a function of the centrality of the collision is correctly reproduced. However, deviations are observed in the case of minimum bias data (top of the figure) concerning fragments with large atomic numbers associated with the most peripheral collisions. There, the results of the calculation are very sensitive to the geometry of the detectors. In particular, a small variation (a fraction of a degree) in the emission angle of the projectilelike can drastically change the charge distribution.

Figure 12 shows the mean kinetic energy of fragments as a function of the atomic number Z. For different beam energies and selections, the kinetic energy distribution is nicely reproduced over the whole atomic number range. For selection (a), which is dominated by peripheral collisions, the kinetic energy of heavy fragments ($Z \geqslant 20$) corresponds essentially to the QT and QP dynamics after deexcitation. In our calculation, it appears that the mean kinetic energy is sensitive to the initial nucleon exchange as well as to the hardness of the potential. Indeed, the values of α_a (Fig. 3) and x_{tr} retained for the simulations have been mainly ad-

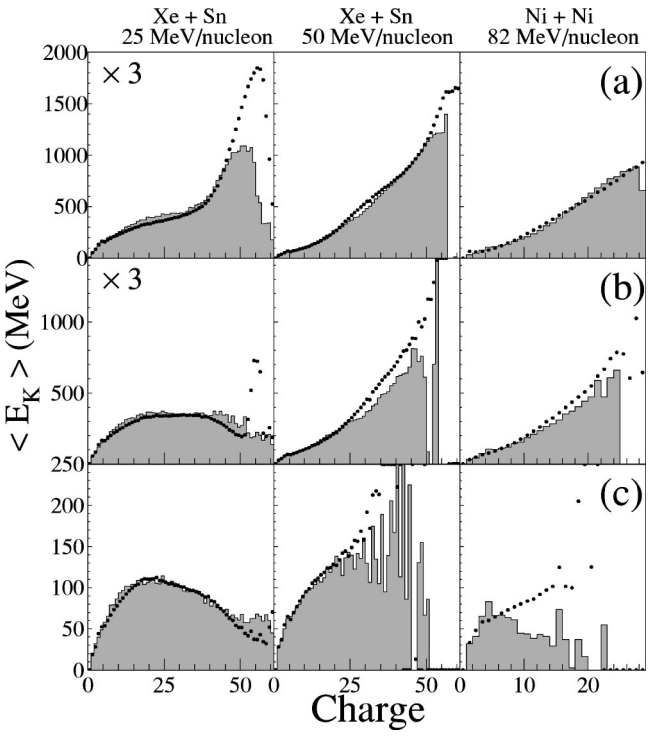

FIG. 12. Mean kinetic energy in the center-of-mass as a function of the charge Z: experimental data (black points), simulated data (filled histograms). Reactions are indicated on top of each panel. Selections are (a), (b), and (c), respectively, from top to bottom.

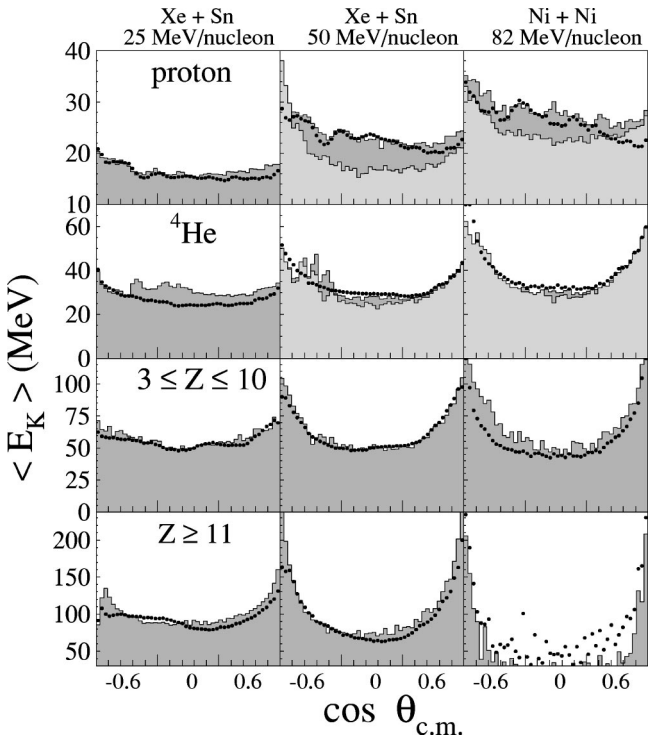

FIG. 13. Mean kinetic energy in the center of mass as a function of the center of mass emission angle. Black points are experimental data while filled histograms are for calculated data. The considered particles and the system under study are indicated in each panel. Events have been selected with the criterium (b). For $E/A=50$ and 82 MeV, we also present in light gray the proton and α particle distributions obtained when nucleon-nucleon collisions are omitted ($x_{\mathrm{coll}}=0\%$).

justed to reproduce Fig. 12. Here, the main effect explaining the kinetic energies is the coupling of the intrinsic motion of the nucleons with the relative velocity between the two partners of the reaction. Since the latter is very close to the initial relative velocity even for central collisions, rather large kinetic energies may be reached. In particular, at low incident energy, the phase of reaggregation is important because the relative velocity between the nascent fragments may be not large enough to overcome the nuclear potential. There is thus a delicate balance between the two energies and it may be that the model is not accurate enough to properly describe this phase in detail. Note that since the kinetic energy is too large, the excitation energy and thus light charged particle multiplicities are underestimated.

We now address the kinematics of light particle and fragment emission by considering more specifically complete events [selection (b) and (c)]. Let us consider event selection (c). These events are associated with central collisions as testified by the results of Fig. 9.

However, the angular distributions of protons, α's, as well as those of IMF's and heavier fragments are anisotropic (not shown here). All in all, the model is able to reproduce the global trends of the data.

The kinematic properties are better evidenced by considering the mean kinetic energy as a function of the center of mass emission angle as displayed in Fig. 13. As far as IMF's and heavy fragments are concerned, a good agreement is achieved between the experimental and simulated data. In particular, the increase of the mean energy for backward/forward angles is reproduced. This trend is a measure of the "memory" of the entrance channel. For light particles, such an anisotropy is also observed. This can be understood because those particles are produced either in the early instants of the collision and, as such, keep a memory of the beam direction or by evaporation on longer time scales. In this last case, they are emitted by "sources" (excited fragments) whose angular distributions are forward/backward peaked and thus they also keep a memory of the entrance channel. Therefore, even for those collisions which are associated with low impact parameters, there is no full stopping of the matter. In our model, there is almost no damping of the nucleon momentum distribution although final state interactions (the reaggregation phase) can lead to a strong rearrangement of the fragment velocity and angular distributions at low incident energy. Therefore, in our picture, fragmentation is a fast off-equilibrium process (a truly transient process) developing on time scales of the order of the reaction time.

However, as the incident energy increases, the mean kinetic energy of the protons and the α's at all emission angles is modified by nucleon-nucleon collisions. Indeed, without such collisions (light gray areas for protons and α particles at $E/A=50$ and 82 MeV in Fig. 13), the average kinetic energy is somehow underestimated, in particular, in the transverse direction. This is particularly true for protons and also for deuterons, tritons, and ^{3}He (not shown). When considering

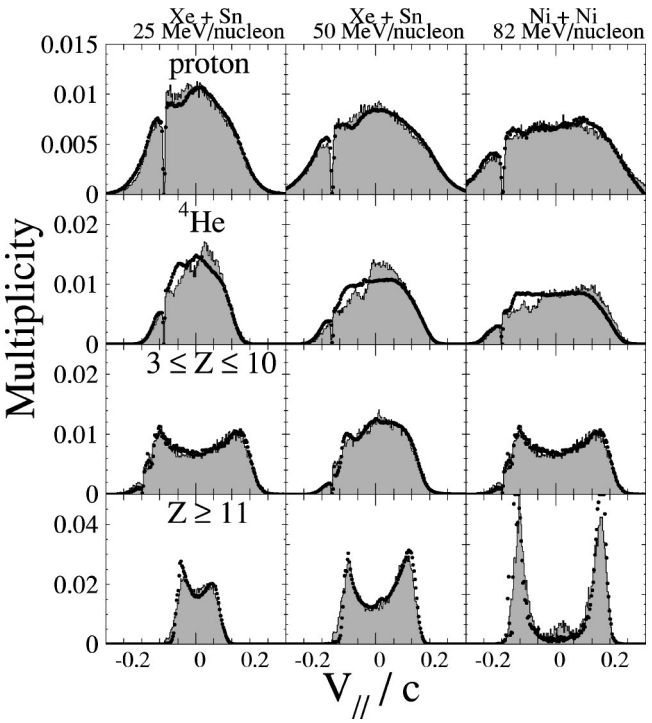

FIG. 14. Experimental (black points) and calculated (filled histograms) $v_{//}$ distributions calculated in the center of mass for different kinds of nuclear species for the three reactions indicated on top of each panel. Event selection: case (b)

nucleon-nucleon collisions (dark gray areas), a systematic increase of the kinetic energy is obtained: this is how the parameter x_{coll} has been adjusted for each incident energy. We therefore believe that the increase in kinetic energy in the transverse direction marks the onset of in-medium nucleon-nucleon collisions. Such collisions become more and more probable as the incident energy increases because the in-medium nucleon phase space opens due to the increasing relative velocity between the two initial Fermi spheres.

E. Midrapidity emission

As a last comparison with experimental data, we now focus on particles and fragments emitted at midrapidity. For fragments with Z lower than 10 (IMF's), a so-called neck emission corresponding to fragments located around midvelocity is expected. This process has now been widely studied in the intermediate energy range. In the framework of the INDRA Collaboration neck emission has been studied for the same system but with a different selection of the data [39,40]. Midrapidity emissions have also been discussed in Refs. [41,42]. A convenient way to put in evidence such an effect is to explore rapidity distributions for various kinds of nuclear species as shown in Fig. 14 corresponding to the event selection (b). A good agreement between the experimental and the simulated data is obtained. In particular, the model can account for the transition between light fragments which are dominantly emitted around midrapidity and heavier species which are essentially remnants of the quasiprojectile and the quasitarget. In this figure, a large excess of light particle emission in the midrapidity region is observed. In our method of initial phase-space sampling, many particles and fragments are produced initially at midrapidity due to the fact that clusters created during the coalescence contain nucleons coming both from the target and the projectile.

IV. CONCLUSIONS AND PERSPECTIVES

In this paper, we have presented an event generator to describe nuclear collisions in the intermediate energy regime at all impact parameters. It is based on a few well-defined hypotheses that can be conveniently and easily tested by a direct comparison with experimental data. In order to illustrate the outputs of the model, we have studied the kinematical characteristics of nuclear products emitted in central as well as peripheral collisions at intermediate energies for medium mass symmetric systems. Data were collected by the INDRA Collaboration at the GANIL facility.

In peripheral and midcentral collisions, the onset of midrapidity emission of both fragments and light particles is accounted for with help of a modified participant-spectator picture in which nucleon transfers are introduced by means of a single parameter. In our approach, as far as multifragmentation is concerned, most clusters are produced rapidly at nearly normal density. As such, they keep a strong memory of the entrance channel. In particular, fragments emerge from the reaction highly deformed in momentum space. Then, they decay sequentially to reach ground state by evaporation on longer time scales by a rearrangement and emission of nucleons and possibly other complex particles. The kinetic energy and angular distributions of both fragments and light charged particles are well reproduced and testify to the strong memory of the entrance channel and to the importance of the internal motion of the nucleons inside the two partners of the reaction. As such, in our picture, the origin of kinetic energy fluctuations is to a large extent nonthermal. We would like to point out that this picture is very similar to the one proposed in Ref. [43]. We thus believe that our model is a valuable alternative to thermal statistical approaches based on shape and/or momentum equilibration in the matter at low density. In particular, in our model, both the collective energy and the deformation often claimed as being necessary to reproduce the data in the framework of thermal statistical models are "naturally" obtained.

Our approach is presently limited around the Fermi-energy range. Deviations between the model and the experimental data are expected when the incident energy increases well above 100 MeV/nucleon. In particular, we do expect that nuclear transparency decreases as the phase space for in-medium nucleon-nucleon collisions increases. Therefore, the two initial Fermi distributions should be progressively more and more relaxed on shorter and shorter time scales as the incident energy increases, thus invalidating the sudden approximation used in our approach. The effect of nucleon-nucleon collisions is actually treated with simple approximations. The complete understanding of two-body effects certainly requires more elaborated treatments.

Although our model is able to reproduce most of the features of the INDRA data considered in this paper, this does

not ensure a general agreement with the data collected in the intermediate energy range. Indeed, the free parameters of the model have been adjusted with help of a limited set of data and additional studies leading to the same values of these parameters are necessary to confirm the validity of our scenario.

In the near future, we plan to extend the model to mass asymmetric systems. Note also that the calculation gives the final charge to mass ratio of fragments created during the reaction and could be a valuable tool to explore the N/Z effects in nuclear collisions in the Fermi-energy range.

Finally, it is worth noting that the technique of exploration of phase space described in this paper is flexible enough to test rapidly other (possibly thermalized) nucleon momentum distributions to describe nuclear fragmentation.

ACKNOWLEDGMENT

We thank warmly INDRA Collaboration for permission to use its data.

[1] D. Durand, E. Suraud, and B. Tamain, *Nuclear Dynamics in the Nucleonic Regime* (IOP, New York, 2001).
[2] J. Pouthas *et al.*, INDRA Collaboration, Nucl. Instrum. Methods Phys. Res. A **357**, 4187 (1995).
[3] L. Moretto and G. Wozniak, Annu. Rev. Nucl. Part. Sci. **43**, 379 (1993); *Proceedings of the XXVII International Workshop on Gross Properties on Nuclei and Nuclear Excitations, Hirshegg, 1999*, edited by H. Feldmeier (GSI, Darmstadt, 1999).
[4] B. Borderie *et al.*, INDRA Collaboration, Eur. Phys. J. A **6**, 197 (1999); M. F. Rivet *et al.*, INDRA Collaboration, Phys. Lett. B **430** 217 (1998).
[5] J. A. Hauger *et al.*, EOS Collaboration, Phys. Rev. C **62**, 024616 (2000).
[6] J. B. Elliot *et al.*, EOS Collaboration, Phys. Rev. C **62**, 064603 (2000).
[7] B. Borderie, J. Phys. G **28**, R217 (2002).
[8] D. H. E. Gross, Rep. Prog. Phys. **53**, 605 (1990).
[9] J. P. Bondorf *et al.*, Phys. Rep. **257**, 133 (1995).
[10] M. D'Agostino *et al.*, Phys. Lett. B **473**, 219 (2000).
[11] S. Ayik and C. Gregoire, Phys. Lett. B **212**, 269 (1988); Nucl. Phys. **A513**, 187 (1990).
[12] J. Randrup and B. Remaud, Nucl. Phys. **A514**, 339 (1990).
[13] A. Guarnera, M. Colonna, and Ph. Chomaz, Phys. Lett. B **373**, 267 (1996).
[14] J. Aichelin, Phys. Rep. **202**, 233 (1991).
[15] H. Feldmeier, K. Bieler, and J. Schnack, Nucl. Phys. **A586**, 493 (1995).
[16] A. Ono, H. Horiuchi, H. Takemoto, and R. Wada, Nucl. Phys. **A630**, 148c (1998).
[17] W. U. Schroder and J. R. Huizenga, in *Treatise on Heavy Ion Science*, edited by A. Bromley (Plenum, New York, 1984), Vol. 2.
[18] G. Casini *et al.*, Phys. Rev. Lett. **67**, 3364 (1991); C. P. Montoya *et al.*, *ibid.* **73**, 3070 (1994); J. Toke *et al.*, *ibid.* **75**, 2920 (1995); J. F. Lecolley *et al.*, Phys. Lett. B **354**, 202 (1995); R. Yanez *et al.*, Phys. Rev. Lett. **82**, 3585 (1999); F. Bocage *et al.*, INDRA Collaboration, Nucl. Phys. **A676**, 391 (2000).
[19] J. Randrup, W. J. Swiatecki, and C. F. Tsang, Lawrence Berkeley Laboratory Report No. LBL-3603, 1974 (unpublished).
[20] J. Blocki, J. Randrup, W. J. Swiatecki, and C. F. Tsang, Ann. Phys. (N.Y.) **105**, 427 (1977).
[21] W. Nörenberg, *Heavy-Ion Collisions* (North-Holland, Amsterdam, 1980), Vol. 2.
[22] D. Lacroix, *Lecture Notes on Macroscopic Aspects of Fusion Reaction* (International Joliot-Curie School, Maubuisson, France, 2002).
[23] D. Vautherin, J. Treiner, and M. Veneroni, Phys. Lett. B **191**, 6 (1987).
[24] P. Ring and P. Schuck, *The Nuclear Many-Body Problem* (Spring-Verlag, New York, 1980).
[25] D. Lacroix and Ph. Chomaz, Nucl. Phys. **A636**, 85 (1998).
[26] W. D. Myers and W. J. Swiatecki, Nucl. Phys. **A601**, 141 (1996).
[27] B. Merlo-Pomorska and K. Pomorski, Z. Phys. A **348**, 169 (1994); B. Merlo-Pomorska and B. Mach, At. Data Nucl. Data Tables **60**, 287 (1995).
[28] Y. Abe, S. Ayik, P.-G. Reinhard, and E. Suraud, Phys. Rep. **275**, 49 (1996).
[29] J. Cugnon *et al.*, Nucl. Phys. **A352**, 505 (1981).
[30] A. Van Lauwe *et al.*, INDRA Collaboration, nucl-ex/0203017.
[31] D. Durand, Nucl. Phys. **A451**, 266 (1992).
[32] J. Brzychczyk and J. Lukasik, Nucl. Phys. **A535**, 273 (1995).
[33] S. Hudan *et al.*, Phys. Rev. C **67**, 064613 (2003); see also the INDRA website: http://infodan.in2p3.fr
[34] A. M. Maskay-Wallez, thesis, University of Lyon (1999); P. Desesquelles *et al.*, INDRA Collaboration, Phys. Rev. C **62**, 024610 (2000); D. Cussol *et al.*, INDRA Collaboration, *ibid.* **65**, 044604 (2002); Ph. Lautesse *et al.*, INDRA Collaboration (submitted).
[35] J. Lukasik *et al.*, INDRA and ALADIN Collaboration, Phys. Rev. C **66**, 064606 (2002).
[36] A. Van Lauwe *et al.* (unpublished)
[37] D. L'Hote and J. Cugnon, Nucl. Phys. **A397**, 519 (1983).
[38] The INDRA Software Filter, INDRA Collaboration (Private communication).
[39] J. Lukasyk *et al.*, INDRA Collaboration, Phys. Rev. C **55**, 1906 (1997).
[40] F. Bocage *et al.*, INDRA Collaboration, Nucl. Phys. **A676**, 391 (2000); J. Colin *et al.*, INDRA Collaboration, Phys. Rev. C **67**, 064603 (2003).
[41] P. Pawlowski *et al.*, INDRA Collaboration, Eur. Phys. J. A **9**, 371 (2000).
[42] D. Dore *et al.*, INDRA Collaboration, Phys. Rev. C **63**, 034612 (2001).
[43] X. Campi, H. Krivine, E. Plagnol, and N. Sator, Phys. Rev. C **67**, 044610 (2003).